

## Simulation of a Laue lens with bent Ge(111) crystals

Vineeth Valsan · Enrico Virgilli ·  
Filippo Frontera · Vincenzo Liccardo ·  
Ezio Caroli · John B Stephen

Received: date / Accepted: date

**Abstract** In the context of Laue project for focusing hard X-/ soft gamma-rays, an entire Laue lens, using bent Ge(111) crystal tiles, with 40 meters curvature radius, is simulated with a focal length of 20 meters. The focusing energy band is between 80 keV and 600 keV. The distortion of the output image of the lens on the focal plane due to the effect of crystal tile misalignment as well as the radial distortion arising from the curvature of the crystal is discussed in detail. Expected detection efficiency and instrument background is also estimated. Finally the sensitivity of the Laue lens is calculated. A quantitative analysis of the results of these simulation is also presented.

**Keywords** Focusing telescopes · X-ray diffraction · Laue lens · Experimental astronomy · High energy instrumentation

### 1 Introduction

Motivated by the astrophysical importance [1] of extending the focusing band up to 600 keV, a project named "LAUE" (supported by the Italian Space Agency) was started with the goal of building Laue lenses[2] for broad energy

---

V. Valsan · E. Virgilli · F. Frontera · V. Liccardo  
Department of Physics, University of Ferrara, Via Saragat 1/c, 44122 Ferrara, Italy  
E-mail: valsan@fe.infn.it  
*Present address:* of V. Valsan  
Indian Institute of Astrophysics, Bangalore 560034, India  
E-mail: vineeth@iiap.res.in

V. Valsan · V. Liccardo  
Université de Nice Sophia-Antipolis, Parc Valrose, 06108 Nice Cedex 2, France

E. Caroli · J. B. Stephen  
IASF-Bologna, INAF, Via Gobetti 101, 40129 Bologna, Italy

band (70-600 keV). Previously, within the project named HAXTEL (Hard X-ray Telescope), two prototypes of Laue lenses made of flat mosaic crystals with short focal length (6m) have been developed and successfully tested [3, 4, 5, 6, 7]. In the framework of LAUE project, a prototype of lens petal made of curved crystals is being developed in the LARIX facility of the Physics and Earth Sciences Department of the University of Ferrara.

Initially, a petal structure of the lens was simulated and built [8, 9]. The simulations made for the petal have been extended to model a complete Laue lens, made of bent Ge(111) crystals, with an energy passband from 90 – 600 keV. Preliminary results have been reported in [10, 11, 12, 13]. Bent crystals, when compared to their flat mosaic counterparts, have higher efficiency and very low mosaicity, i.e., curved crystals have high diffraction efficiency and a better capability of concentrating the signal collected over a large area into a small focal spot. In this paper, the details of this simulation with the results will be discussed.

## 2 Simulating the entire Laue lens

The simulation uses bent Ge(111) crystal tiles with radius of curvature equal to 40 meters (i.e. twice the lens focal length) and the dimension of each tile is  $30 \times 10 \times 2 \text{ mm}^3$ . The quasi-mosaic crystal has a mosaicity of 4.12 arcsec. The bending technology adopted for Ge is the surface grooving [14]. From the dynamical theory of diffraction of bent crystals, it results that the bending of a perfect crystal creates a curvature of the lattice planes (111) of Ge, with a ratio between the internal curvature and external curvature radii of 2.39 [15]. This gives rise to a quasi-mosaic configuration of the bent crystal. This effect is not valid for all lattice planes. For example, if the diffracting planes in transmission configuration are (220), the quasi-mosaicity is not created.

The advantages offered by bent crystals are that their reflectivity exceeds the theoretical limit of 50%, valid for flat perfect and mosaic crystals. The focusing capability is also better when the crystal is bent [16]. Experimental tests confirm the expectations [8].

The simulation of the entire Laue lens provides the space distribution of the focused photons in the focal plane (Point Spread Function, PSF) for on-axis photons. It takes into account

- the ideal case (without any distortions or misalignments);
- different values of misalignment (in arcsec) in the positioning of the crystal tile on the lens frame and radial distortions (in meters) from the required curvature radius of 40 meters.

This investigation will help us in determining the acceptable level of distortion to get a reasonable PSF.

## 2.1 Effect of tile misalignment

Each crystal tile is positioned on the lens petal frame with an orientation such that the image of the beam reflected by the crystal is formed on the lens focus, where there is the position sensitive focal plane detector.

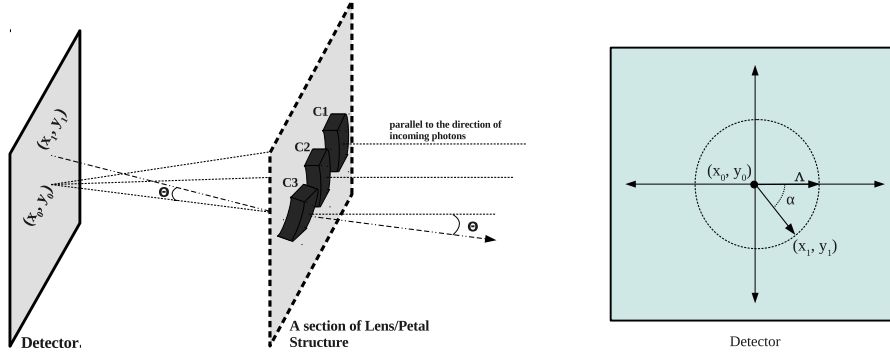


**Fig. 1** Misalignment in the positioning of the crystals on the lens petal frame deviates the PSF. *Left* figure illustrates this effect.  $(x_0, y_0)$  is the position on the detector where the center of the image formed by the reflection of X-rays through perfectly positioned crystals (C1 & C2) falls. When there is a misalignment of  $\Theta$  arcsec in the positioning (crystal C3), the center of the image is formed at  $(x_1, y_1)$ . The figure on the *right* shows the focal plane (where there is the detector) with these positions.

When a crystal having a misalignment from its proper position, the image of that crystal on the detector will have a deviation. In Fig. 1, let  $(x_0, y_0)$  be the center of the image formed by the reflection of rays from a crystal, which is perfectly positioned on the lens petal frame without any misalignment.  $(x_1, y_1)$  is the position of the center of the image formed by a crystal having a misalignment of  $\Theta$  arcsec with respect to its proper positioning. Crystals C1 and C2 are perfectly positioned, while crystal C3 has a misalignment of  $\Theta$  arcsec. The center of its image is formed on the detector at  $(x_1, y_1)$ . The deviation of the center of the image from  $(x_0, y_0)$  to  $(x_1, y_1)$  is shown on the right side of Fig. 1. For a given misalignment of  $\Theta$  arcsec, the linear deviation  $\Lambda$  is given by:

$$\Lambda = f \Theta \quad (1)$$

where  $f$  ( $= 20$  meters) is the focal length of the lens.

Given that there is a uniform probability of having the point  $(x_1, y_1)$  over the locus of the circle with center at  $(x_0, y_0)$  and a radius of  $\Lambda$ , the angle  $\alpha$  (see Fig. 1, *right*) is expected to have a uniform distribution.

The expected misalignment,  $\Theta$ , is of the order of few arcsec. The effects of this misalignment have been incorporated in the code, with a uniform distribution.

## 2.2 Effect of radial distortion

Figure 2 illustrates the effect of radial distortion ( $R_{dist}$ ) on the PSF. The width of the PSF is equal for a symmetrical deviation of the curvature radius from its expected value. That is, if  $R_p$  is the expected value of the curvature radius, and  $\Delta R$  is the distortion from the expected value, the width of the PSF is equal for a curvature radius of  $R_p + \Delta R$  or  $R_p - \Delta R$ .

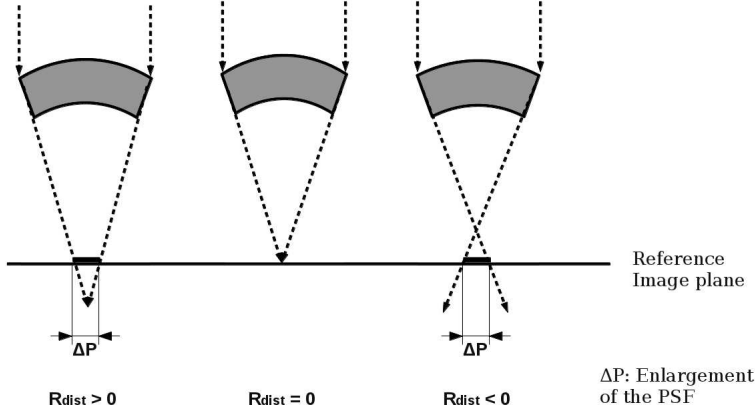


**Fig. 2** The effect of radial distortion ( $R_{dist}$  or  $R_d$ ) on the PSF of the lens.

In Fig. 3,  $R_p$  is the expected primary curvature radius,  $f (= 2R_p)$  is the corresponding focal length.  $R_s = 2.39R_p$ , is the secondary curvature radius corresponding to  $R_p$ .  $R_{dist} = R_p + \Delta R$ ,  $\Delta R$  being the distortion in curvature radius.  $f_d$  is the focal length corresponding to  $R_{dist}$ .  $R_{sd} = 2.39R_{dist}$ , is the secondary curvature radius corresponding to  $R_{dist}$ . At the focal distance,  $f$ , the width  $W$  of the PSF is given by the angle  $\beta$  of the secondary curvature (see Fig. 3):

$$W = f \frac{dim_1}{R_s} = f\beta$$

Similarly at  $f_d$ , the width  $W_{fd}$  is given by  $W_{fd} = \beta_d f_d$ , where  $\beta_d = \frac{dim_1}{R_{sd}}$ .  $W_d$  is the width of the image formed on the detector placed on the focal plane at a distance  $f$ , and can be derived as follows.

From Figure 3,

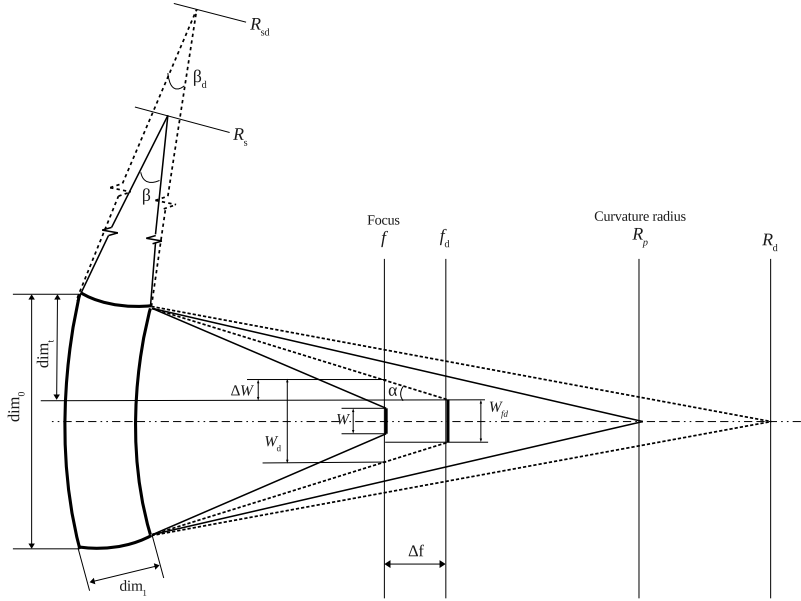


**Fig. 3** Diagram illustrating the effect of radial distortion of bent Ge(111) crystal on the width of the PSF.

$$dim_t = \frac{dim_0 - W_{fd}}{2}$$

$$\alpha = \frac{dim_t}{f_d}$$

$$\Delta f = |f_d - f|$$

$$\Delta W = \Delta f \alpha$$

$$W_d = W_{fd} + 2\Delta W$$

For the statistical approach in the code, the same methodology used for the misalignment effect has been adopted also for the radial distortion. The range of radial distortion is assumed to be uniformly distributed over all the crystals. For example, for a maximum radial distortion of 6 meters, the code incorporates this effect with a uniform distribution of the deviation of the radius in the range  $[0, 6)$  meters from the expected curvature radius of 40 meters.

Ring-by-ring details of the lens are given in Table 1. Different parameters and their corresponding values are given in Table 2.

The simulation results are shown in Fig. 4, 5, 6 and 7. The energy band is from 80 keV to 600 keV. The *left* panels show the image of the PSF, while the *right* panels show the 3D plot.

**Table 1** Ring-by-ring characteristics of the lens made by Ge(111) crystal tiles.

Ring	Radius (cm)	No. of crystal tiles	Min. Energy (keV)	Max. Energy (keV)	Energy range (keV)
1	12.673	79	535.609	679.409	143.799
2	15.673	98	442.047	535.608	93.560
3	18.673	117	376.312	442.047	65.734
4	21.673	136	327.596	376.311	48.714
5	24.673	155	290.048	327.596	37.547
6	27.673	173	260.222	290.047	29.825
7	30.673	192	235.958	260.221	24.263
8	33.673	211	215.833	235.957	20.124
9	36.673	230	198.871	215.833	16.961
10	39.673	249	184.381	198.871	14.489
11	42.673	268	171.859	184.381	12.521
12	45.673	286	160.930	171.859	10.928
13	48.673	305	151.308	160.929	9.621
14	51.673	324	142.771	151.307	8.535
15	54.673	343	135.146	142.770	7.624
16	57.673	362	128.295	135.146	6.850
17	60.673	381	122.104	128.294	6.189
18	63.673	400	116.484	122.104	5.619
19	66.673	418	111.358	116.483	5.125
20	69.673	437	106.664	111.357	4.693
21	72.673	456	102.350	106.663	4.313
22	75.673	475	98.371	102.349	3.977
23	78.673	494	94.690	98.371	3.680
24	81.673	513	91.275	94.690	3.414
25	84.673	532	88.097	91.274	3.176
26	87.673	550	85.134	88.097	2.963
27	90.673	569	82.363	85.133	2.770
28	93.673	588	79.767	82.362	2.595

**Table 2** Parameters of the lens made by Ge(111) crystal tiles.

Parameter	Value
Focal length	20 meters
Energy range	80 - 600 keV
Subtended angle	18 degree
No. of Rings	28
Minimum radius	12.67 cm
Maximum radius	93.67 cm
No. of crystal tiles	9341
Crystal material	Ge(111)
Crystal dimension	30 mm $\times$ 10 mm $\times$ 2 mm
Crystal mass (total)	2.07 g $\times$ 9341 = 19.335 kg

### 3 Quantitative analysis of the simulation results

This section deals with the quantitative analysis of the results obtained from the simulations and their consequences. In particular we discuss the radial

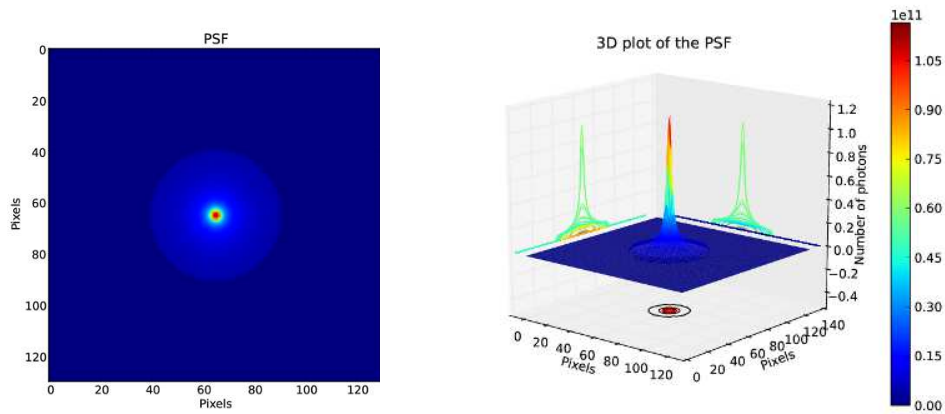


**Fig. 4** PSF of the lens made with Ge(111) without any misalignment errors and also with no radial distortion. Each pixel is having a dimension of  $200\mu \times 200\mu$ .

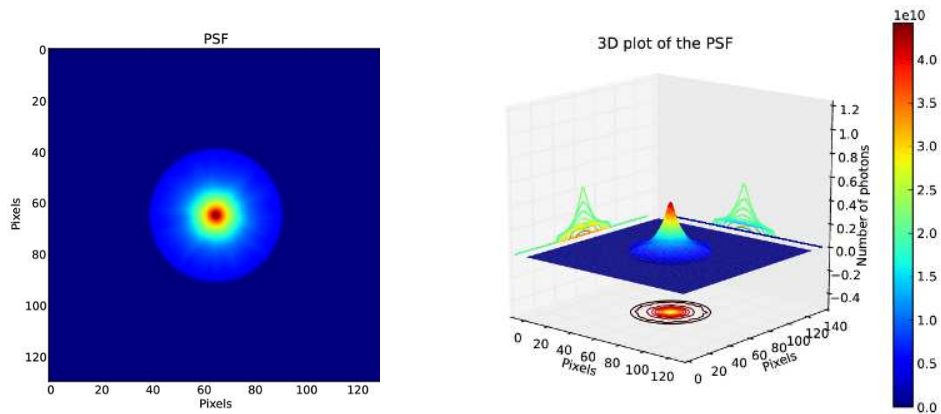


**Fig. 5** PSF of the lens made with Ge(111) without any misalignment errors but with a maximum radial distortion of 6 meters. Each pixel is having a dimension of  $200\mu \times 200\mu$ .

profile of the enclosed photons, the achievable effective area, the sensitivity for both continuum and lines of the complete lens.

### 3.1 Full Width at Half Maximum (FWHM) of the PSF

Any misalignment in the positioning of the crystal on the lens frame and also any distortion in the curvature radius affects the FWHM of the PSF.

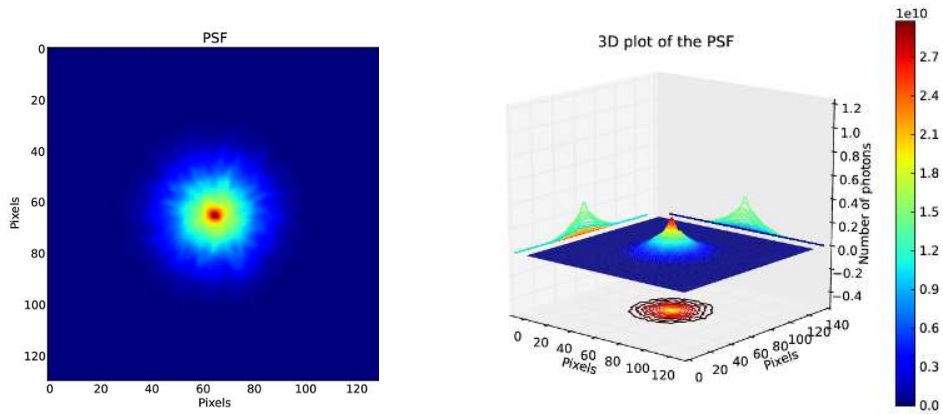


**Fig. 6** PSF of the lens made with Ge(111) with a maximum misalignment of 30 arcsec and without any radial distortion. Each pixel is having a dimension of  $200\mu \times 200\mu$ .

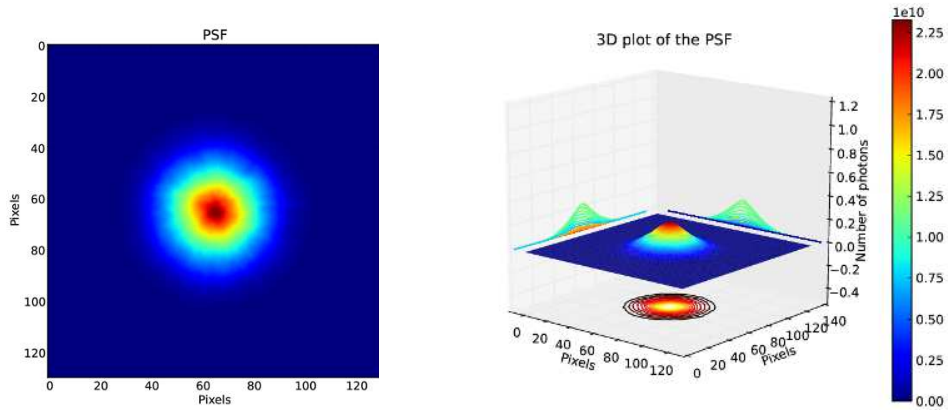


**Fig. 7** PSF of the lens made with Ge(111) with a maximum misalignment of 30 arcsec and with a maximum radial distortion of 6 meters. Each pixel is having a dimension of  $200\mu \times 200\mu$ .

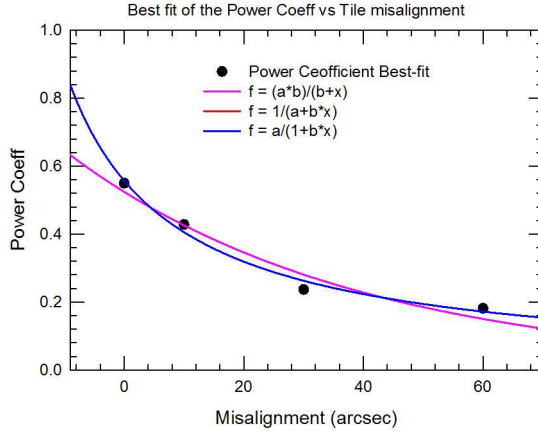
Figure 9 shows the FWHM profiles of the simulated lens as function of the radial distortion. Each value (in meters) reported on the  $x$ -axis corresponds to the maximum value of the uniformly distributed radial distortion,  $[0, x)$  meters, from the ideal radius of 40 meters. Each line in the plot represents the corresponding value of maximum misalignment in the positioning of the crystal tile (shown in the legend of the plot).



The model used for fitting is a power law with a threshold and having two free parameters.

$$FWHM = a(1 + RD)^c \quad (2)$$

For this model the best-fit values of the parameter seems more correlated with the tiles misalignments: the parameter  $a$  reproduce directly the minimum achievable FWHM for perfect tile alignment, while the power coefficient,  $c$  decrease monotonically as the tile misalignment level increase.



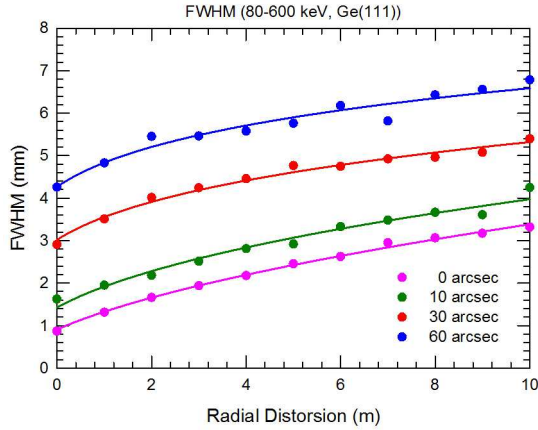
**Fig. 8** Best fit of the power coefficient vs tile misalignment.

Fig. 8, shows the tentative models that has been considered to fit the power law coefficient of the model shown in Eqn. 2, to obtain a semi-empirical relationship to evaluate a-priori the FWHM starting from the values expected for the case of perfect tile alignment on the lens support. In the graph the last two function used (red line and blue line) are perfectly superimposing and therefore, at least in the considered interval of misalignments, are equivalent. In any case, these two model describe better the behaviour of the power coefficient as a function of tile misalignment (correlation coefficient is  $> 0.99$  and the standard error of estimate is about 0.026). The parameters for these last two fit are:

$$a = 1.80 \pm 0.08, b = 0.067 \pm 0.009; \text{ for } f = 1/(a + bx) \text{ and}$$

$$a = 0.56 \pm 0.02, b = 0.037 \pm 0.006; \text{ for } f = a/(1 + bx)$$

As can be seen from Fig. 9, the FWHM of the PSF increases with the misalignment value as well as with the radial distortion. When there is no misalignment and no radial distortion, that is, when the lens is perfectly built, the FWHM is 0.6 mm, which is that expected for a single crystal tile.



**Fig. 9** FWHM profile of the lens made with Ge(111) for different values of crystal misalignment and radial distortion. The values in the legend shows maximum misalignment (in arcsec) in the positioning of crystals.

### 3.2 Peak intensity and radial profile

Any misalignment in the positioning of the crystal on the lens frame and also any distortion in the curvature radius from the required value of 40 meters will also affect the peak intensity of the PSF. This effect is plotted in Fig. 10. The peak intensity, as expected, gets reduced with the increase of the crystal misalignment and radial distortion. With respect to a perfect lens made of Ge(111) without any misalignment or radial distortion, the peak intensity gets reduced to 20% for a maximum misalignment of 30 arcsec and a maximum radial distortion of 6 meters. This is also evident from the comparison of Fig. 4 with Fig. 7.

The PSF radial profile is obtained by calculating the total photons radially enclosed outwards from the focal point of the PSF. The PSF profile of the lens made of Ge(111) with perfect alignment of the crystal tiles and no radial distortion is shown in Fig. 11. The values of the radius (in both pixels and mm) for a given enclosed percentage of photons, are reported in the Table 3.

### 3.3 Effective area

The effective area of a lens made of crystals at an energy  $E$  is defined as the product of the geometric area of the crystals that reflect photons in a narrow energy interval  $\Delta E$  around  $E$   $\left(E - \frac{\Delta E}{2} \leq E \leq E + \frac{\Delta E}{2}\right)$  times the mean reflection efficiency in this energy interval.

In our case, if the entire energy range (90-600 keV) of the lens is subdivided into 10 equal bins in logarithmic scale, the total geometric area in

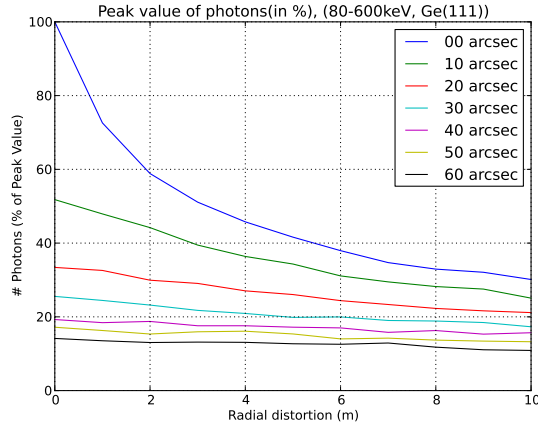


**Fig. 10** Peak intensity profile of the petal made with Ge(111) for different values of crystal misalignments and radial distortion. The values in the legend shows maximum misalignment (in arcsec) in the positioning of crystals.

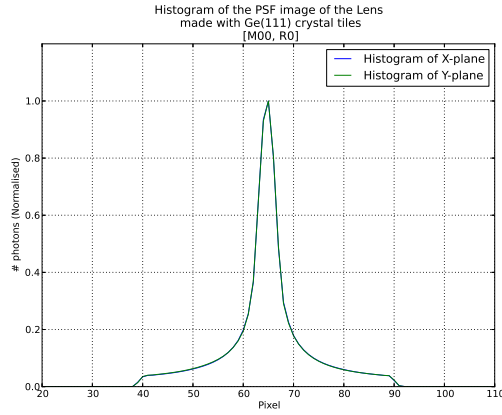


**Fig. 11** PSF profile of the lens made of crystal tiles of Ge(111). A perfect positioning of the crystal tiles and no radial distortions are assumed.

the  $i^{th}$  energy bin,  $G_{total}^{bin}$ , is the total cross section of the crystals that reflect photons in the energy range of the bin.

For example, if  $E_{min}^{bin}$  and  $E_{max}^{bin}$  are respectively the minimum and maximum energy of a given bin, then the total geometric area  $G_{total}^{bin}$ , in this energy bin is given by:

$$G_{total}^{bin} = \pi(R_{max}^2 - R_{min}^2) \quad (3)$$

**Table 3** Radial distribution of the enclosed photons for a perfect positioning of the crystal tiles without any radial distortion.

Enclosed photons (%)	Radius	
	(pixels)	(mm)
10	3	0.6
20	4	0.8
30	5	1.0
40	6	1.2
50	7	1.4
60	8	1.6
70	10	2.0
80	12	2.4
90	14	2.8
100	20	4.0

where, through the Bragg law,

$$R_{max} = \frac{hcf}{d_{hkl}E_{min}^{bin}}$$

$$R_{min} = \frac{hcf}{d_{hkl}E_{max}^{bin}}$$

If  $N_c(\Delta E)$  is the number of crystal tiles that reflect photons in a given energy bin, and  $A_{xtal}$  is the surface area ( $dim[0] \times dim[1]$ ) of a single crystal tile, then Eqn.3 can also be written as

$$G_{total}^{bin} = N_c(\Delta E) \times A_{xtal} \quad (4)$$

Hence, in this method, the total geometric area  $G_{total}^{bin}$ , does not depend upon the thickness as well as the mosaicity of the crystal tile.

The effective area  $A_{eff}^{bin}$ , in a given energy bin is given by:

$$A_{eff}^{bin} = G_{total}^{bin} \times \mathfrak{R} \quad (5)$$

where  $\mathfrak{R}$  is the mean reflectivity in that bin.

The large values of effective area at lower energies and smaller values at higher energies are due to the difference in the number of crystal tiles corresponding to those energies. For example, the number of Ge(111) crystal tiles corresponding to lowest energy bin (in case of  $\Delta E$  sub-divided into 10 logarithmically equal bins) are around 2092, but there are only 68 Ge(111) crystal tiles corresponding to the highest energy bin.

Table 4 gives the values of different parameters that have been derived for the effective area calculation.

**Table 4** The values of different parameters for each of the 10 logarithmic energy bins for the lens made with Ge(111) crystal tiles.

Energy range (keV)	$R_{max}$ (cm)	$R_{min}$ (cm)	$\Delta R$ (cm)	$G_{total}^{bin}$ ( $cm^2$ )	$\mathfrak{R}$	$A_{eff}^{bin}$ ( $cm^2$ )
90 – 109	84.35	69.64	14.70	7113.75	0.57394	4082.90
109 – 132	69.64	57.51	12.13	4848.13	0.69485	3368.75
132 – 159	57.51	47.74	9.76	3229.57	0.77453	2501.40
159 – 193	47.74	39.33	8.41	2301.14	0.82582	1900.32
193 – 233	39.33	32.58	6.75	1525.71	0.85862	1310.01
233 – 281	32.58	27.01	5.56	1042.1	0.87979	916.83
281 – 340	27.01	22.32	4.68	726.78	0.89458	650.16
340 – 411	22.32	18.47	3.85	494.4	0.90532	447.60
411 – 496	18.47	15.30	3.16	335.89	0.91055	305.85
496 – 599	15.30	12.67	2.63	231.34	0.90075	208.38

### 3.4 Continuum Sensitivity

It is well known that continuum sensitivity of a focusing telescope in the observation time  $T_{obs}$  and in the energy band  $\left(E - \frac{\Delta E}{2}, E + \frac{\Delta E}{2}\right)$ , is given by

$$I_{ft}^{min}(E) = n_{\sigma} \frac{\sqrt{B(E)}\sqrt{A_d}}{\eta_d f_{\epsilon} A_{eff} \sqrt{\Delta E} \sqrt{T_{obs}}} \quad (6)$$

where the instrument background is assumed to be Poissonian, and

- $n_{\sigma}$  is the number of standard deviations  $\sigma$ ,
- $B(E)$  is the intensity of the instrument background (in  $counts/s/cm^2/keV$ ) at the energy  $E$ ;
- $\eta_d$  is the efficiency of the position sensitive detector;
- $f_{\epsilon}$  is the fraction of photons that is focused on the detector area  $A_d (= \pi R_{spot}^2)$ ;
- $T_{obs}$  is the observation time;
- $A_{eff}$  is the mean effective area in the energy band  $\left(E - \frac{\Delta E}{2} \leq E \leq E + \frac{\Delta E}{2}\right)$  of the telescope optics.

### 3.5 Expected detection efficiency and instrument background

As discussed in our paper by Khalil et al. [17], a Germanium detector is a good candidate as focal plane position sensitive detector of the focused photons, with a pixel size of  $350 \mu m \times 350 \mu m$ , a cross section of  $10 \times 10 cm^2$  and a thickness of 12.5 cm or higher. In such a way a high detection efficiency (80%) can be achieved up to the highest energies of the lens pass band (650 keV).

The detector efficiency  $\eta_d$  behaviour adopted for the simulations is shown in Fig. 12.

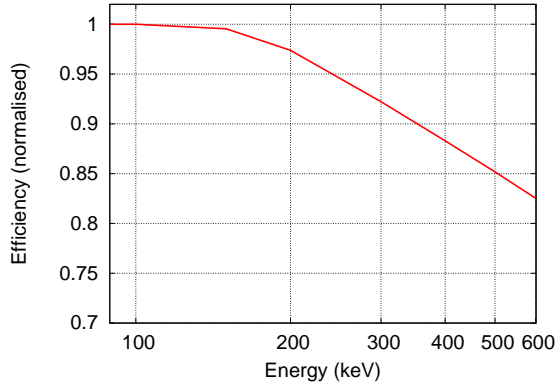


**Fig. 12** Detection efficiency behaviour with energy of the Ge stacked detector adopted for the simulations.

Concerning the instrument background, for our simulations the Laue lens is assumed to be placed in a Low Earth Orbit (LEO). Following the same procedure discussed in our paper by Khalil et al.[17], from the background data in the energy band from 90 – 600 keV measured by SPI instrument onboard the INTEGRAL satellite in High Earth Orbit, we have derived the background level expected for the lens. The result is shown in Fig. 13. In addition to the expected lens background, the SPI measured background is shown, for comparison.

By inserting in the Eqn. 6 the background level and detection efficiency given above, we can get the continuum sensitivity of the simulated Laue lens. Figure 14 shows the result, at  $3\sigma$  level for an observation time  $T_{obs} = 10^5$ s and  $\Delta E = E/2$ , along with the continuum sensitivity of other missions.

From this figure it is apparent that at 100 keV, the simulated lens is 4 orders of magnitude more sensitive than INTEGRAL IBIS. Similar results are obtained when we compare the lens with the other INTEGRAL instrument SPI. The data of ISGRI and SPI are taken from the reference [18] and [19], respectively. At about 511 keV, for a lens made with Ge(111), the continuous sensitivity is more than 2 orders of magnitude better than IBIS.

### 3.6 Sensitivity to narrow emission lines

The sensitivity to narrow emission lines is derived by superposing the emission line to the continuum source level. In the case of a lens telescope, if the source continuum level can be accurately determined, the minimum detectable intensity  $I_L^{min}$  (in *photons/s/cm<sup>2</sup>*), of a line is given by

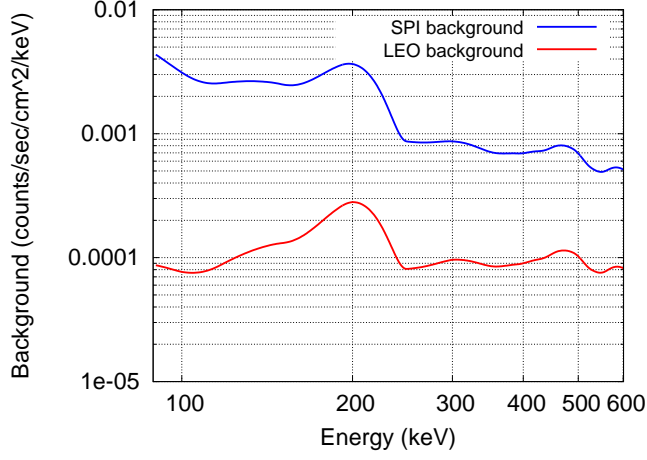


**Fig. 13** The expected lens background at LEO, compared with the INTEGRAL SPI measured background.

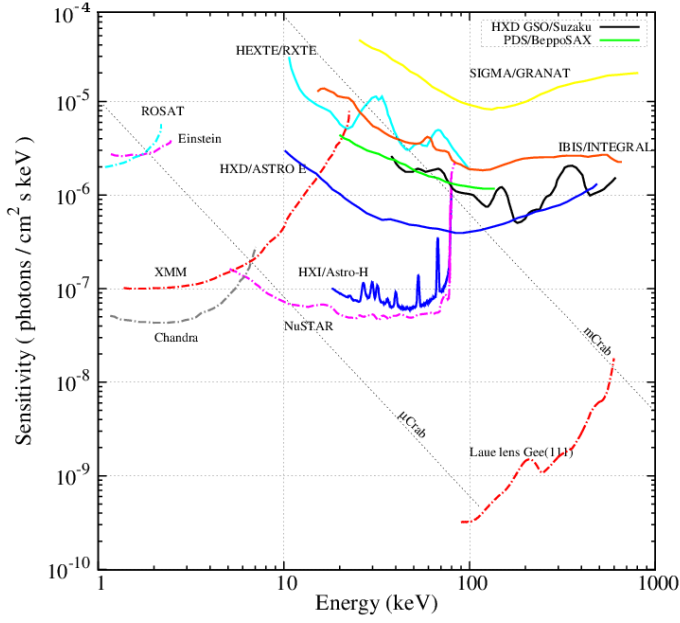


**Fig. 14** Sensitivity of different missions. Continuous line shows the direct-view instruments/missions. Dashed line depicts the focusing instruments/missions.

$$I_L^{min}(E_L) = 1.31n_\sigma \frac{\sqrt{[2B(E_L)A_d + I_c(E_L)\eta_d f_\epsilon A_{eff}] \Delta E}}{\eta_d f_\epsilon A_{eff} \sqrt{T_{obs}}} \quad (7)$$

where  $B(E_L)$  is the intensity of the measured background spectrum (in counts/s/cm<sup>2</sup>/keV) at the line energy  $E_L$ ;  $I_c(E_L)$  is the source continuum intensity (in photons/s/cm<sup>2</sup>/keV) at the centroid of the line,  $A_{eff}$  is the lens effective area at an energy  $E_L$ ,  $A_d$  is the detection area that encloses  $f_\epsilon = 50\%$  of the focused photons (half power), and  $\Delta E$  is the FWHM of the line profile around  $E_L$ . The  $\Delta E$  value depends upon the energy resolution of the detector. We have assumed  $\Delta E = 2$  keV (expected for our simulated detector), detector area  $A_d$  corresponding to the half power radius given in Table 3,  $\eta_d$  shown in Fig. 12, and  $A_{eff}$  derived from Eqn. 5 with a filling factor of 0.2 mm.

The result at different energies and for an observation time of  $10^5$  s and  $10^6$  s is shown in Table 5.

**Table 5**  $3\sigma$  line sensitivity (in photons/s/cm<sup>2</sup>) of a lens with time of observation times of  $10^5$  and  $10^6$ .

Energy (keV)	$T_{obs} = 10^5 \text{ sec}$	$T_{obs} = 10^6 \text{ sec}$
100	$1.08 \times 10^{-8}$	$3.26 \times 10^{-9}$
200	$3.31 \times 10^{-8}$	$1.04 \times 10^{-8}$
300	$7.19 \times 10^{-8}$	$2.27 \times 10^{-8}$
400	$1.47 \times 10^{-7}$	$4.67 \times 10^{-8}$
511	$2.39 \times 10^{-7}$	$7.55 \times 10^{-8}$

**Table 6**  $3\sigma$  line sensitivity (in photons/s/cm<sup>2</sup>) of ISGRI and of SPI (observation time =  $10^6$  seconds,  $\Delta E = E/2$ ).

ISGRI		SPI	
Energy (keV)	Line sensitivity (photons/s/cm <sup>2</sup> )	Energy (keV)	Line sensitivity (photons/s/cm <sup>2</sup> )
112.9	$1.67 \times 10^{-5}$	100	$4.4 \times 10^{-5}$
225.4	$3.21 \times 10^{-5}$	–	–
449.6	$6.64 \times 10^{-5}$	–	–
566.1	$8.40 \times 10^{-5}$	500	$3.1 \times 10^{-5}$

For comparison, in Table 6 we report the line sensitivity at different energies and for an observation time of  $10^6$  s shown by IBIS and SPI aboard INTEGRAL. It can be seen that the lens expected sensitivity, at about 100 keV, is 4 orders of magnitude better, and, at 511 keV, is 3 orders of magnitude better.



## 4 Conclusions

A complete Laue lens made of Ge(111) crystal tiles is simulated and modeled, with an energy passband from 90 – 600 keV. The on-axis PSF, its FWHM, effective area and sensitivity (to continuum and to narrow emission lines) of the entire Laue lens have been modeled. The sensitivity results show that this lens is almost 3 orders of magnitude more sensitive than ISGRI [18] and SPI [19] on-board the INTEGRAL satellite.

With the sensitivity that this lens is expected it can achieve, many fundamental open astrophysical cases [1] can be settled.

**Acknowledgements** Vineeth Valsan acknowledges the support from Erasmus Mundus Joint Doctorate Program by Grant Number 2010-1816 from the EACEA of the European Commission. The LAUE project is the result of huge efforts of large number of organizations and people. We would like to thank all of them. We also acknowledge the ASI (Italian Space Agency) for its support to the LAUE project under contract I/068/09/0. Currently, V. Valsan is supported by India-TMT Project.

## References

1. F. Frontera, E. Virgilli, V. Valsan, V. Liccardo, V. Carassiti, E. Caroli, F. Cassese, L.R.C. Ferrari, V. Guidi, M. Pecora, S.Mottini, L. Amati, N. Auricchio, L. Bassani, R. Campana, R. Farinelli, C. Guidorzi, C. Labanti, R. Landi, A. Malizia, M. Orlandini, V. Sguera, J.B. Stephen, L.G. Titarchuk, (2013), *Society of Photo-Optical Instrumentation Engineers (SPIE) Conference Series*, vol. 8861
2. F. Frontera, P.V. Ballmoos, astro-ph.IM (2011). DOI arXiv:1007.4308v3. URL arXiv:1007.4308v3
3. F. Frontera, E. Virgilli, V. Liccardo, V. Valsan, V. Carassiti, S. Chiozzi, F. Evangelisti, S. Squerzanti, M. Statera, V. Guidi, C. Ferrari, R.A. Zappettini, E. Caroli, N. Auricchio, S. Silvestri, R. Camattari, F. Cassese, L. Recanatesi, M. Pecora, S. Mottini, B. Negri, (2012), *Society of Photo-Optical Instrumentation Engineers (SPIE) Conference Series*, vol. 8443. DOI 10.1117/12.926378
4. F. Frontera, E. Virgilli, V. Liccardo, V. Valsan, V. Carassiti, F. Evangelisti, S. Squerzanti, G. Risaliti, *Journal of Physics Conference Series* **355**(1), 012005 (2012)
5. E. Virgilli, F. Frontera, V. Valsan, V. Liccardo, V. Carassiti, F. Evangelisti, S. Squerzanti, (2011), *Society of Photo-Optical Instrumentation Engineers (SPIE) Conference Series*, vol. 8147. DOI 10.1117/12.895233
6. E. Virgilli, F. Frontera, V. Valsan, V. Liccardo, E. Caroli, J.B. Stephen, F. Cassese, L. Recanatesi, M. Pecora, S. Mottini, P. Attiná, B. Negri, (2011), *Society of Photo-Optical Instrumentation Engineers (SPIE) Conference Series*, vol. 8147
7. V. Valsan, E. Virgilli, V. Liccardo, F. Frontera, in *X-ray Astrophysics up to 511 keV* (2011)
8. V. Liccardo, E. Virgilli, F. Frontera, V. Valsan, (2012), *Society of Photo-Optical Instrumentation Engineers (SPIE) Conference Series*, vol. 8443. DOI 10.1117/12.926364
9. V. Valsan, F. Frontera, E. Virgilli, V. Liccardo, (2012), *Society of Photo-Optical Instrumentation Engineers (SPIE) Conference Series*, vol. 8443. DOI 10.1117/12.926301
10. V. Liccardo, E. Virgilli, F. Frontera, V. Valsan, V. Guidi, E. Buffagni, (2013), *Society of Photo-Optical Instrumentation Engineers (SPIE) Conference Series*, vol. 8861. DOI 10.1117/12.2023617
11. V. Valsan, F. Frontera, E. Virgilli, V. Liccardo, E. Caroli, J.B. Stephen, (2013), *Society of Photo-Optical Instrumentation Engineers (SPIE) Conference Series*, vol. 8443
12. E. Virgilli, F. Frontera, V. Valsan, V. Liccardo, V. Carassiti, F. Evangelisti, S. Squerzanti, M. Parise, M. Statera, v. Guidi, , V. Bellucci, R. Camattari, E. Caroli, N. Auricchio,

- 
- A. Basili, S. Silvestri, J.B. Stephen, F. Cassese, L. Recanatesi, C. Ferrari, A. Zappettini, E. Buffagni, S. Mottini, M. Pecora, B. Negri, (2013), *Society of Photo-Optical Instrumentation Engineers (SPIE) Conference Series*, vol. 8861
13. V. Valsan, Extending the band of focusing x-ray telescopes beyond 100 keV: Motivations and proposed solutions. Ph.D. thesis, University of Ferrara-Italy (2013)
  14. V. Guidi, V. Bellucci, R. Camattari, I. Neri, (2011), *The Second Ferrara Workshop on "X-ray Astrophysics up to 511 keV*, vol. 28
  15. V. Bellucci, R. Camattari, V. Guidi, *Astronomy and Astrophysics* **560**, 59 (2013)
  16. V. Guidi, V. Bellucci, R. Camattari, I. Neri, *Journal of Applied Crystallography* **44**(6), 1255 (2011)
  17. M. Khalil, F. Frontera, E. Caroli, E. Virgilli, V. Valsan, *Nuclear Instruments and Methods in Physics Research Section A: Accelerators, Spectrometers, Detectors and Associated Equipment* **786**(0), 59 (2015)
  18. G. Blanger, *INTEGRAL IBIS Observers Manual*. ESA, 1st edn. (2012)
  19. C.S. Fernandez, *INTEGRAL SPI Observers Manual*. ESA, 1st edn. (2012)